Journal of Materials Chemistry A

Accepted Manuscript

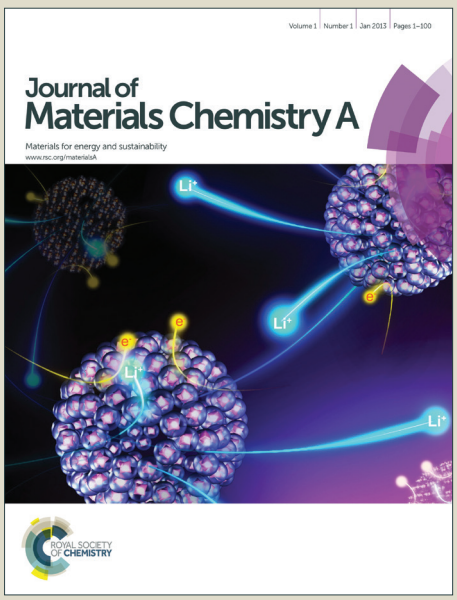

ROYAL SOCIETY OF CHEMISTRY

www.rsc.org/materialsA

Unique Z-Scheme 2D/2D Nanosheet Heterojunction Design to Harness Charge Transfer for Photocatalysis

Huijie Cheng,[a] Jungang Hou,[ab*] Osamu Takeda,[b] Xing-Min Guo,[a] Hongmin Zhu[ab]

[a]School of Metallurgical and Ecological Engineering, University of Science and Technology Beijing, Beijing 100083, China

[b]Tohoku University, 6-6-02 Aramaki-Aza-Aoba, Aoba-ku, Sendai, 980-8579 Japan

Corresponding author: jhou@ustb.edu.cn

ABSTRACT:

The heterojunction photocatalysts could provide a potential strategy to solve the serious energy and environmental crises. However, the required heterojunction photocatalyts with high charge-separation efficiency and strong redox ability, which have unique dimensionality-dependent integrative and synergic effects are intriguing but still underdeveloped. Here, we design and fabricate the first 2D/2D heterojunctions between carbon nitride nanosheet and oxygen-vacancies confined in bismuth titanate mesoporous nanosheet. Especially, selective pollutant transformations of rhodamine B and 4-chlorophenol solution under visible-light irradiation have been conducted by use of 2D/2D heterojunction photocatalysts.

Based on the steady-state and transient photoluminescence spectra and electron spin resonance technology, the Z-scheme energy-transfer mechanism is identified and the photogenerated charge carriers in the 2D/2D heterojunctions display the prolonged lifetime and higher separation than those in carbon nitride and bismuth titanate alone. This work will shed light on the rational design of more complex 2D/2D heterojunctions with accompanying applications in solar energy conversion and environmental remediation fields.

KEYWORDS: Nanosheet; 2D/2D Heterojunction; Charge Transfer; Photocatalysis

1. Introduction

Environmental purification and energy conversion on the basis of highly efficient photocatalysts and solar energy attract more and more attention.[1-3] To date, a large number of photocatalysts have been explored for the purpose of efficient degradation of harmful organic substances and hydrogen evolution via water splitting.[4-10] Although it is very effective under near-UV light irradiation, conventionally applied TiO_2 photocatalyst is not ideal for this purpose because TiO_2 performs rather poorly in the processes associated with solar photocatalysis. However, the practical application of this material is still hindered by its main disadvantage of wide band gap (~3.2 eV for anatase), resulting in only a small ultraviolet (UV) fraction (~4.0%) of solar spectrum that can be used to initiate photochemical reactions.[2] In order to more

efficiently utilize solar energy, a variety of visible-light-responsive semiconductors are being developed as the future generation of photocatalysts.

Many Bi- and Ti-containing compounds, such as $Bi_4Ti_3O_{12}$, $Bi_{12}TiO_{20}$, and $Bi_{20}TiO_{32}$, have attracted much attention due to their layered structure and the resulting unique physical properties.[11-16] For example, $Bi_{12}TiO_{20}$ nanostructures and their photocatalytic activity under visible-light irradiation have been systematically investigated in our group.[14,15] However, it is hard to produce highly crystalline and single phase $Bi_{20}TiO_{32}$ because different bismuth titanate phases are formed depending on different chemical compositions and processing conditions. Metastable $Bi_{20}TiO_{32}$ photocatalysts by use of α-Bi_2O_3 and anatase TiO_2 as raw materials were synthesized by a high-temperature quenching method, resulting into an irregular morphology and large agglomerated particles as well as a low surface area due to high temperatures.[16] Especially, developing low-dimensional semiconductor photocatalysts, is becoming an important strategy to improve their photocatalytic activity and/or tune their reaction preferences toward different applications.[17,18] Especially, various two-dimensional semiconductors are a conceptually-new class of materials, which provide promising opportunities to satisfy the requirement of various nanodevices.[19] Thus, facet engineering fully exposed with reactive facets is an exciting direction for developing highly active bismuth titanate photocatalysts.

In addition to the classic semiconductor photocatalysts, a fascinating metal-free sustainable photocatalyst, graphite-like carbon nitride (g-C_3N_4),

due to its remarkable physical and chemical properties has recently attracted worldwide attention due to its polymeric π-conjugated structure.[20] For example, g-C_3N_4 exhibits an appealing electronic structure with bandgap of 2.7 eV that allows a maximal light absorption in the visible-light region (400~460 nm). Nonetheless, metal-free g-C_3N_4 suffers from disadvantages such as rapid recombination of electrons and holes as well as low visible-light utilization efficiency.[7] Accordingly, the development of reliable and facile strategies to fabricate g-C_3N_4-based photocatalysts with unique photocatalytic performances is of growing interests. As a result, g-C_3N_4-based heterostructured photocatalysts such as g-C_3N_4/TiO_2, CoO_x/C_3N_4/TaON, g-C_3N_4/ZnO, g-C_3N_4/Bi_2WO_6, g-C_3N_4/$BiVO_4$, and g-C_3N_4/g-C_3N_4 have been constructed, and the enhanced photocatalytic activity of heterojunctions with respect to g-C_3N_4 is revealed due to the fast separation and transportation.[21-27]

For further improving the visible-light photocatalytic activity of g-C_3N_4 or $Bi_{20}TiO_{32}$, we herein report our attempts to explore the area of 2D/2D heterojunctions for photocatalytic application. g-C_3N_4 and bismuth titanate, which serve as the efficient photocatalysts, were chosen as the building blocks for the construction of 2D/2D heterojunctions. However, to the best of our knowledge, there is no systematic study on the construction and visible-light photocatalytic performance of 2D metastable bismuth titanate nanosheets coupled with 2D carbon nitride nanosheets as an integrated 2D/2D heterojunctions. Among the various heterojunctions with the tunable dimentionalities (0D/2D, 1D/2D and 2D/2D), the

2D/2D type heterojunction often exhibits the higher charge mobility and low charge recombination rates due to the larger interface region with face-to-face contact.[28,29] Herein, in this work, we gave a successful attempt to construct the 2D/2D heterojunction photocatalysts through coupling the g-C_3N_4 (CN) nanosheets with oxygen vacancies confined in $Bi_{20}TiO_{32}$ (BTO) mesoporous nanosheets with exposed {001} facets by a facile hydrothermal process in assistance with post-treatment (Fig. 1). It is demonstrated that the lifetimes of photogenerated charge carriers of 2D BTO mesoporous nanosheets could be prolonged by approximately millisecond timescales after a proper weight ratio of 2D carbon nitride nanosheets is coupled, leading to the promoted charge separation with Z-scheme energy-transfer mechanism, which has been identified by the steady-state and transient photoluminescence spectra and electron spin resonance technology. This is responsible for the unexpected high photocatalytic activity for pollutant degradation under visible light irradiation. This work will shed light on the rational design of more complex 2D/2D heterojunctions with accompanying applications in solar energy conversion and environmental remediation fields.

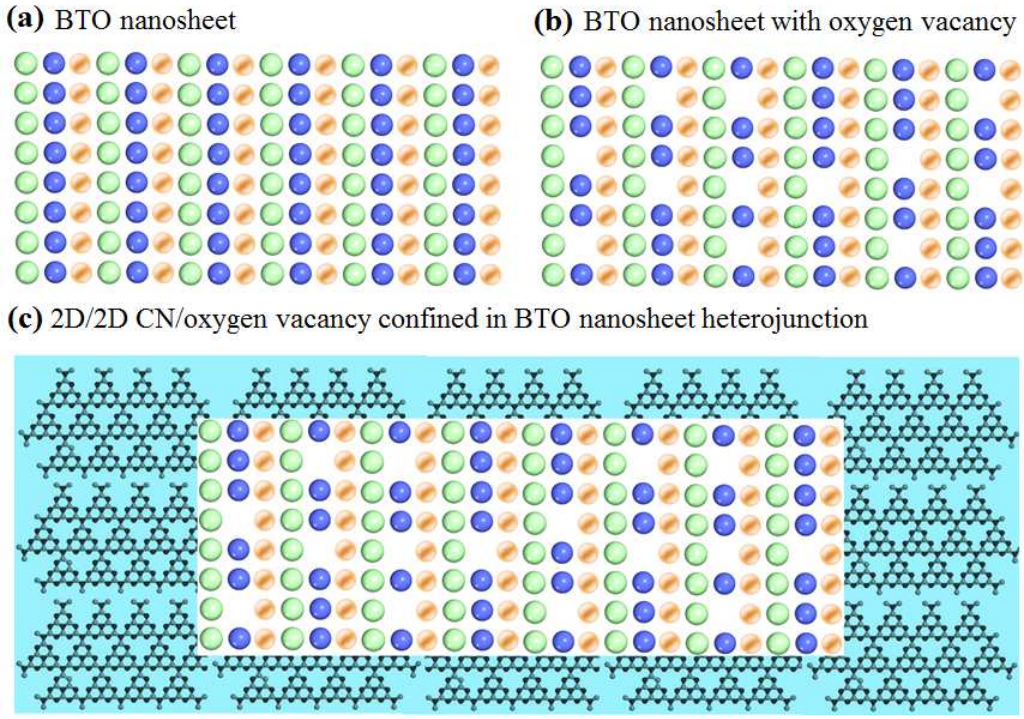

Fig. 1 Schematic illustration of (a) 2D BTO nanosheet, (b) 2D oxygen-vacancy confined in BTO nanosheet, and (c) 2D/2D carbon nitride/oxygen-vacancy confined in BTO nanosheet heterojunction.

2. Experimental section

2.1 Fabrication of 2D/2D $C_3N_4/Bi_{20}TiO_{32}$ nanosheet heterojunctions

All chemicals were analytical grade and used without further purification. Bulk C_3N_4 was synthesized by directly heating low-cost melamine.[35] In detail, 5 g of melamine powder was put into an alumina crucible with a cover, then heated to 500 ^oC in a muffle furnace for 4 h at a heating rate of 20 ^oC/min to obtain the bulk C_3N_4. Then, 30 mg of bulk C_3N_4 was dispersed in 100 mL isopropyl alcohol at room temperature and exfoliated by ultrasonication for 12 h. The resultant

dispersions were centrifuged at 3000 rpm for 10 min. After centrifugation, the supernatant (exfoliated C_3N_4 nanosheets, about top five sixths of the centrifuged dispersion) was collected by pipette. Namely, the exfoliated C_3N_4 (CN) nanosheets were obtained (Fig. 2a).

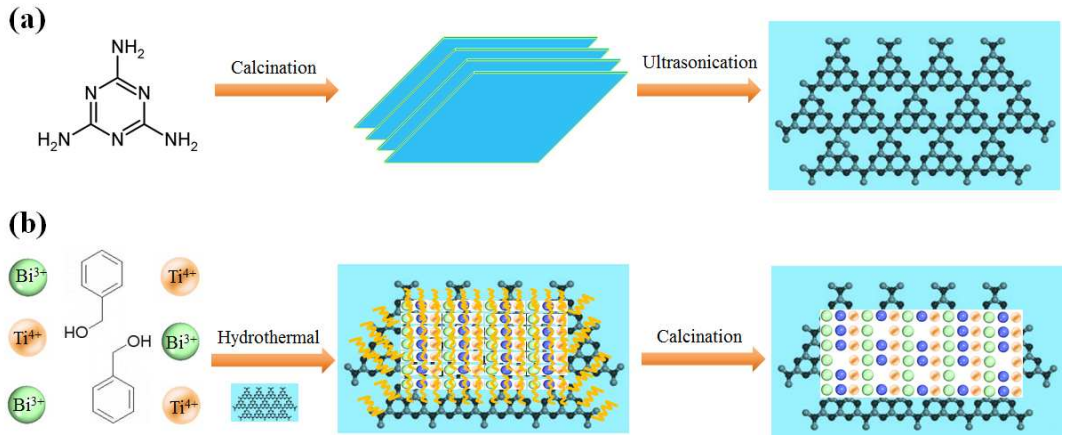

Fig. 2 Schematic illustration of fabrication of (a) 2D carbon nitride nanosheet, and (b) 2D/2D carbon nitride/oxygen-vacancies-confined in bismuth titanate nanosheet heterojunctions.

In a typical procedure, C_3N_4 nanosheets with tunable weight, 3.64 g $Bi(NO_3)_3 \cdot 5H_2O$, 0.18 mmol $Ti(OC_3H_7)_4$ and $NaBH_4$ were dissolved in 15 mL of benzyl alcohol under vigorous stirring. The hydrothermal synthesis was conducted at 120 °C for 24 h in an electric oven by the use of Teflon-lined stainless autoclave (50 mL capacity). The system was then cooled to ambient temperature naturally. The as-prepared samples as precursors were collected and washed with distilled water and absolute alcohol several times, vacuum-dried, and then heated at 300 ^oC

for 5 h to obtain 2D/2D $C_3N_4/Bi_{20}TiO_{32}$ (CN/BTO) heterojunctions (Fig. 2b). In comparison, bulk $Bi_{20}TiO_{32}$ sample was prepared by a high-temperature quenching method using α-Bi_2O_3 and anatase TiO_2 as raw materials.[29]

2.2 Characterization

The obtained products were characterized by powder X-ray diffraction (XRD, MAC Science Co. Ltd Japan) using Cu Ka (λ = 0.1546 nm) and XRD patterns were obtained at 10~80 2θ by step scanning with a step size of 0.02°. The morphology and size of the resultant products were observed by transmission electron microscopy (TEM, JEM-2010). The FT-IR and Raman spectras were recorded on Nexus 470 FT-IR spectrometer and Spex 403 Raman spectrometer. The chemical states of the sample were determined by X-ray photoelectron spectroscopy (XPS) in a VG Multilab 2009 system (UK) with a monochromatic Al Ka source and a charge neutralizer. The optical properties of the samples were analyzed by UV-vis diffuse reflectance spectroscopy (UV-vis DRS, UV-2550, Shimadzu) in the range 200~900 nm. Nitrogen adsorption-desorption isotherms were obtained on a nitrogen adsorption apparatus (ASAP 2020, USA) with all samples degassed for 12 h prior to measurements. Electron spin resonance (ESR) signals of spin-trapped paramagnetic species with 5,5-dimethyl-l-pyrroline N-oxide (DMPO) were recorded with a Bruker A300E spectrometer. DMPO/H_2O and DMPO/CH_3OH were prepared by the conventional method. The photoluminescence spectra were measured with a fluorescence spectrophotometer (F-7000, Japan) using a Xe lamp as excitation source with optical filters. Time-resolved photoluminescence (PL)

spectroscopy was recorded on FLsp920 Fluorescence spectrometer (Edinburgh Instruments) with excitation at 420 nm.

2.3 Photocatalytic test

Photocatalysis reactions were performed in an air-free, closed gas circulation system with a quartz reaction cell. Photocatalytic activity was evaluated by the degradation of rhodamine B (RhB) and 4-chlorophenol (4-CP) in aqueous solution under visible-light irradiation using a 300 W Xe lamp with a cutoff filter ($\lambda > 420$ nm). A cylindrical Pyrex flask (200 mL) was placed in a sealed black box of which the cutoff filter was set on the window face of the reaction vessel to ensure the desired irradiation condition. In each experiments, the samples as catalysts (0.1 g) were added into rhodamine B (RhB) and 4-chlorophenol (4-CP) solution ($1*10^{-4}$ M, 100 mL). The suspension between photocatalyst powders and rhodamine B (RhB) and 4-chlorophenol (4-CP) at given time intervals (3 mL aliquots) were sampled and centrifuged to remove photocatalysts. The filtrates were analyzed by recording the variations of the absorption-band maximum in the UV-vis spectra of RhB and 4-CP in aqueous solution using a UV-vis spectrophotometer (Shimadzu 2550, Japan).

3. Results and discussion

The crystal structures of the samples were analyzed by XRD pattern, as shown in Fig. 3. It is evident that as-prepared products can be indexed to well crystallized $Bi_{20}TiO_{32}$ structure (PDF NO. 42-202) with the major peaks at 2θ = 28.02, 31.62,

32.88, 46.26, 54.16, 55.77 and 57.91°, corresponding to the diffractions of the (201), (002), (220), (222), (203), (421), and (402) planes of the tetragonal $Bi_{20}TiO_{32}$ structure.[13,16] With the increase of the weight ratio of C_3N_4 up to 20wt%, there is no obvious change in the major peaks for CN/BTO hybrids whilst the gradual decreasing intensity of CN/BTO hybrids exist in this case.

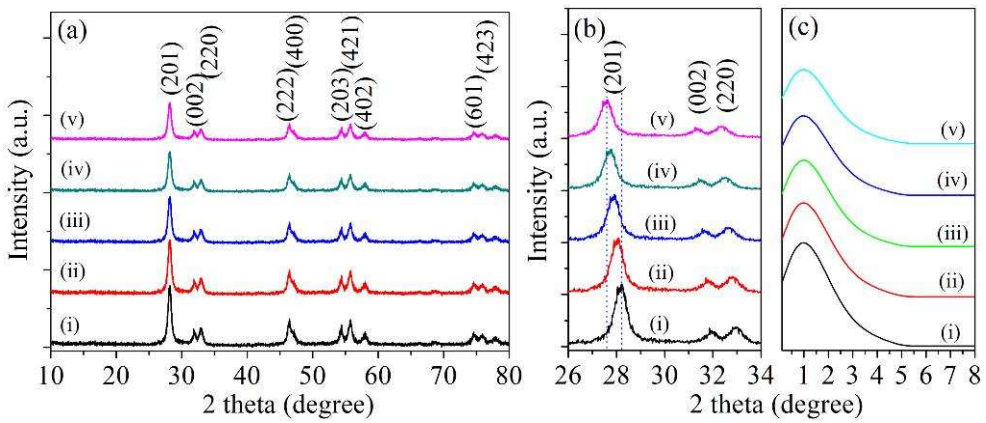

Fig. 3 (ab) XRD patterns and (c) small-angle XRD patterns of as-prepared various hybrids. (i) BTO; (ii) 5wt% CN/BTO; (iii) 10wt% CN/BTO; (iv) 15wt% CN/BTO; and (v) 20wt% CN/BTO heterojunctions.

Compared with XRD pattern of pure BTO, the characteristic peaks of BTO in the CN/BTO hybrids are shifted to smaller diffraction angle for 0.6° indicating that the strong inter-reaction between CN and BTO phase. It is also seen that the crystal phase of BTO did not change after hybridization with CN but the diffraction peak positions for CN/BTO are located at slightly lower angles than those for BTO, suggesting a strong interaction between BTO and CN. Moreover, no other impurity phase was seen, indicating the CN/BTO is a two phase composite. Especially, all

these samples showed a single intense broad peak with no distinctive higher order peaks in their respective small-angle powder XRD patterns, corresponding to an apparent peak at low 2θ value (*ca.* 1°) for mesostructural ordering of CN/BTO hybrids, which is in agreement with the size distribution of mesoporous structure of CN/BTO hybrids (Fig. S1).

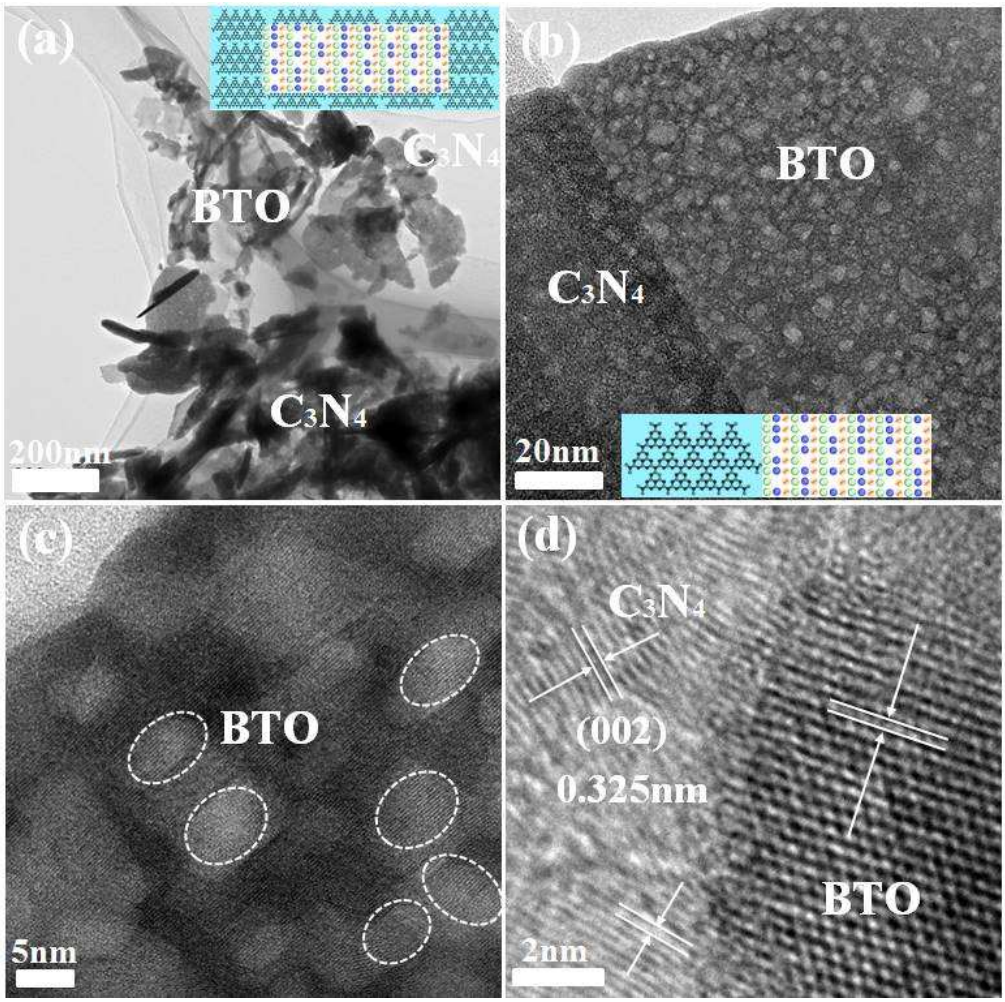

Fig. 4 TEM images of as-prepared 15wt% CN/BTO nanosheet heterojunctions.

The TEM images of as-synthesized 15wt% CN/BTO nanosheet heterojunctions were shown in Fig. 4. This kind of open mesoporous architecture, with a two-dimentional connected pore system, is a desirable feature of catalyst design. The high-resolution TEM image in Fig. 4 clearly revealed the high {001} orientation of the $Bi_{20}TiO_{32}$ sheets. More importantly, the TEM images also depicted that the pits possessed an occupancy in the $Bi_{20}TiO_{32}$ sheets, indicating the presence of abundant pit-surrounding Bi and Ti sites. Oppositely, the attached nanosheets on the $Bi_{20}TiO_{32}$ sheets show low crystallinity with apparent lattices of 0.325 nm, which is the typical characteristic of g-C_3N_4.[21-27] As shown in Fig. 4bd, notably, the two phases contact with each other through a well-defined boundary, indicating the formation of high quality heterojunction structures.

To investigate in-depth the atomic structure of BTO and 15wt% CN/BTO heterojunction, the Fourier transform infrared and Raman spectra were carried out in Fig. 5 and Fig. S2~S4. In the case of BTO nanosheets, two absorption bands were observed at 590 and 813 cm^{-1} in the IR spectra of BTO (Fig. 5a and Fig. S2), which can be ascribed to the stretching vibration of Ti–O band, confirming the formation of crystalline BTO. In 15wt% CN/BTO hybrid, the peak at 1636 cm^{-1} is attributable to C=N stretching vibration modes, while the 1238, 1313 and 1400 cm^{-1} are related to aromatic C–N stretching,[30,31] which is similar to those of the main peaks of pure g-C_3N_4 wavenumber. Especially, all of the main characteristic peaks of g-C_3N_4 move to a higher wavenumber, indicating that the bond strengths of C=N and C–N become weaker which indicates that the conjugated system of

g-C_3N_4 has been stretched and a more widely conjugated system composed by g-C_3N_4 and $Bi_{20}TiO_{32}$ has appeared.[30,31] Thus, the FT-IR reveals the presence of g-C_3N_4 in the heterojunctions and there are weak covalent bonds between g-C_3N_4 and $Bi_{20}TiO_{32}$. Moreover, Raman spectra of 15wt% CN/BTO heterojunctions is similar to those of the main peaks of pure g-C_3N_4 wavenumber. As shown in Fig. 5b and Fig. S3~S4, all of the main characteristic peaks of g-C_3N_4 move to a higher wavenumber.[32] Especially, the characteristic peaks around 1100, 1138, 1217 and 1296 cm^{-1} in the 15wt% CN/BTO heterojunctions indicate the presence of g-C_3N_4 in the heterojunctions.

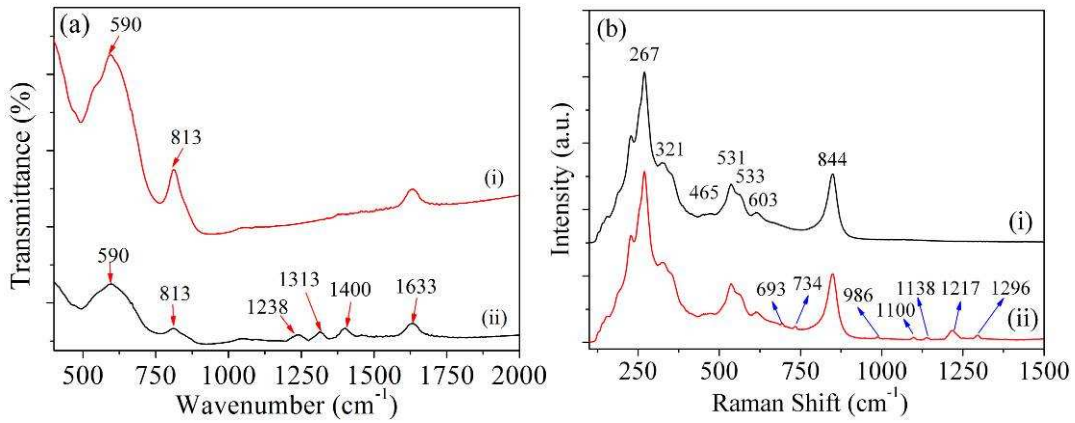

Fig. 5 FT-IR and Raman spectra of as-prepared (i) BTO nanosheets and (ii) 15wt% CN/BTO nanosheet heterojunctions.

In order to reveal the very essential part of the BTO and 15wt% CN/BTO nanosheet heterojunctions, the chemical states of as-prepared BTO nanosheets were carefully checked by the X-ray photoelectron spectroscopy (XPS), as shown in Fig.

6. The Bi 4f fine XPS spectra of the BTO and 15wt% CN/BTO heterojunctions is presented in Fig. 6a. XPS signals of Bi 4f were observed at binding energies at around 164.3 eV (Bi $4f_{5/2}$) and 158.9 eV (Bi $4f_{7/2}$) ascribed to Bi^{3+}.[13,16] XPS signals of Ti 2p of the BTO and 15wt% CN/BTO heterojunctions were observed at binding energies at around 464.4 eV (Ti $2p_{1/2}$) and 458.6 eV (Ti $2p_{3/2}$).[13,16] The XPS signals of Bi 4f and Ti 2p of the BTO and 15wt% CN/BTO heterojunctions indicate the existance of BTO phase. Moreover, XPS signals of C 1s and N 1s of the CN and 15wt% CN/BTO heterojunctions were observed. The appearance of the new C 1s peak at 288.2 eV (Fig. 6c) and the blue shift of N 1s peak at 398.6 eV (Fig. 6d) indeed indicate that the g-C_3N_4 structure has changed after interaction with BTO to form the heterojunction,[33] which can confirm the existence of chemical bonds between CN and BTO in the heterojunctions. Moreover, two peaks can also be clearly identified from the O 1s core level spectra shown in Fig. 6e: one peak at 529.8 eV is deemed as the oxygen bond of Bi−O−Ti, while the other located at 531.3 eV can be attributed to the O-atoms in the vicinity of O-vacancy.[34] However, the peak area of 531.3 eV is widely different, indicating that the bismuth titanate mesoporous nanosheets possess O-vacancies compared with bulk bismuth titanate counterpart. To further confirm the existence of oxygen vacancies, in situ electron paramagnetic resonance (EPR) of 15wt% CN/BTO samples was performed, as shown in Fig. 6f. It can provide a sensitive and direct method to monitor various behaviors of the presence of oxygen defects.[31] The intensity of the EPR signal atg ~2.001 of O-vacancies confined in bismuth titanate mesoporous nanosheets is

much higher than that of bulk BTO under the same conditions. As reported previously, the peak at g~2.001−2.004 can be attributed to netural oxygen vacancies about the surface.[31] After the introduction of CN nanosheets, there is no obvious change for the O-vacancies in the 15wt% CN/BTO heterojunctions. Thus, the aforementioned XPS and ESR spectra demonstrate that the 2D/2D heterojunctions are composed of CN nanosheets and oxygen-vacancy-confined in bismuth titanate mesoporous nanosheets.

The specific surface area of BTO and 15wt% CN/BTO heterojunctions were investigated by nitrogen adsorption-desorption analysis, as shown in Fig. 7a. The specific surface area of 15wt% CN/BTO nanosheet heterojunctions is 52 m^2 g^{-1} which is much higher than that of BTO nanosheets (26 m^2 g^{-1}). The corresponding Barrett−Joyner−Halenda (BJH) analyses (the inset in Fig. 7a) exhibit that most of the pores fall into the size range from 3 to 55 nm. These pores presumably arise from the spaces among the 15wt% CN/BTO nanosheet heterojunctions. The high surface area and mesoporous structure of the 15wt% CN/BTO nanosheet heterojunctions provide the possibility for the efficient diffusion and transportation of the degradable organic molecules and hydroxyl radicals in photochemical reaction, which will lead to the enhanced photocatalytic performance of the CN/BTO nanosheet heterojunctions.

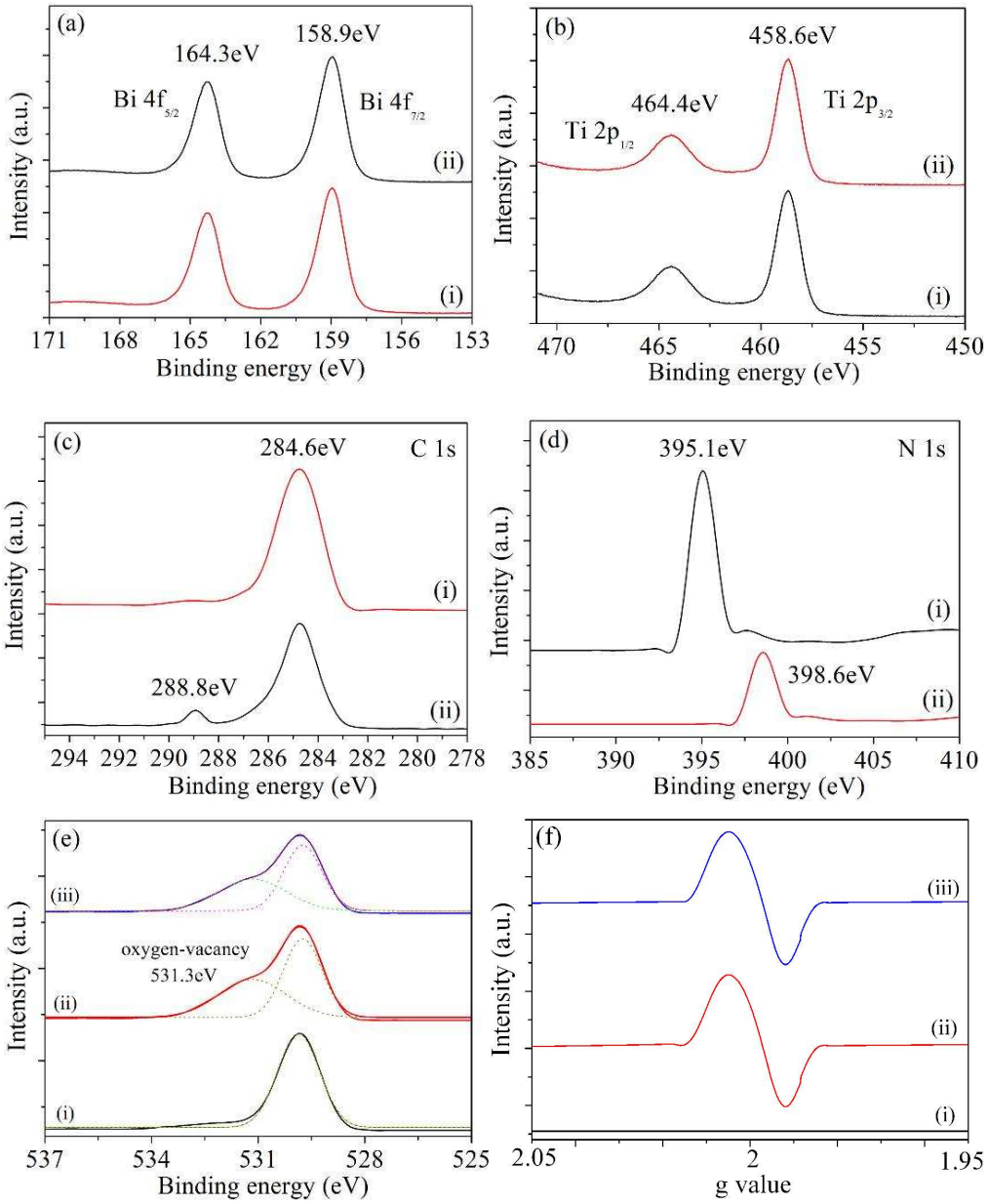

Fig. 6 High resolution XPS spectra of (a) Bi 4f, (b) Ti 2p, (c) C 1s, (d) N 1s for (i) CN and (ii) 15wt% CN/BTO, (e) O 1s for (i) bulk BTO, (ii) BTO and (iii) 15wt% CN/BTO and (f) ESR spectra of (i) bulk BTO, (ii) BTO and (iii) 15wt% CN/BTO.

The optical absorption of the BTO and 15wt% CN/BTO nanosheet heterojunctions was measured by UV−vis diffuse reflection spectroscopy, as shown in Fig. 7b. The O-vacancy confined in BTO nanosheets presented the wavelength range up to 550 nm for the visible light absorption. After the introduction of g-C_3N_4 nanosheets, the absorption spectra onset of 15wt% CN/BTO with the different weight ratio is 500~600 nm and the UV−vis absorption of the 15wt% CN/BTO heterojunction shows the enhanced light scattering in the visible-light region. Thus, it is considered that utilizing visible light for driving photocatalytic reactions is a key challenge and visible light absorption of a material is a prerequisite for visible light performance.

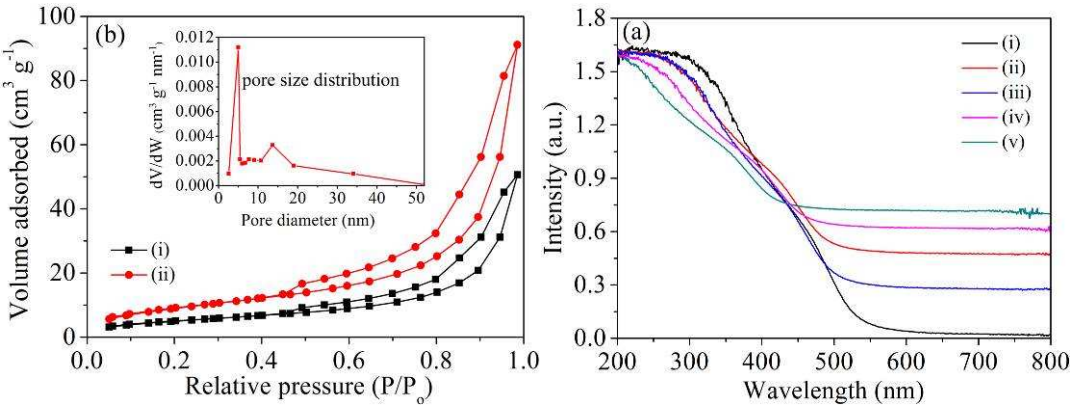

Fig. 7 (a) BET specific surface area of (i) BTO and (ii) 15wt% CN/BTO heterojunctions. Inset of pore-size distribution of 15wt% CN/BTO heterojunctions. (b) UV-Vis spectra of various hybrids. (i) BTO, (ii) 5wt% CN/BTO, (iii) 10wt% CN/BTO, (iv) 15wt% CN/BTO, and (v) 20wt% CN/BTO heterojunctions.

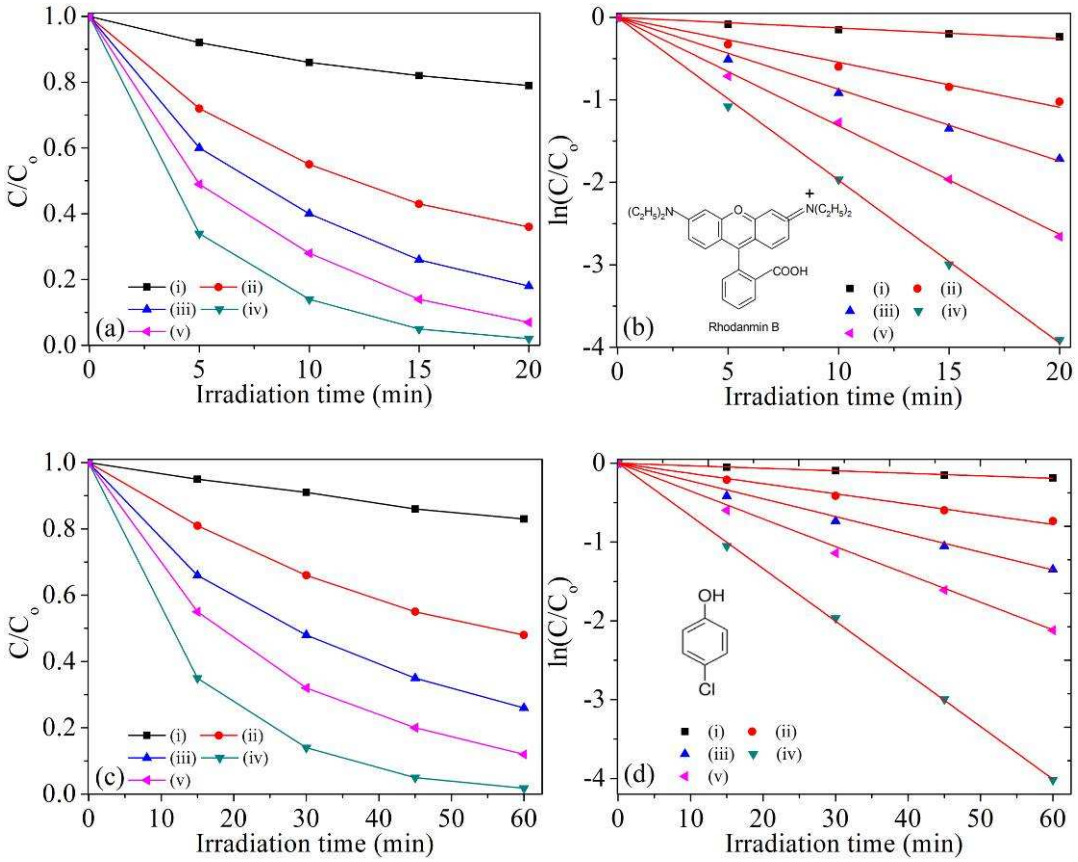

Fig. 8 Photocatalytic degradation curves (ac) and kinetic linear simulation curves (bd) of RhB (ab) and 4-CP (cd) over as-fabricated products under visible light irradiation. (i) BTO; (ii) 5wt% CN/BTO; (iii) 10wt% CN/BTO; (iv) 15wt% CN/BTO; and (v) 20wt% CN/BTO heterojunctions.

The photocatalytic activities of the as-prepared 2D BTO and 2D/2D CN/BTO nanosheet heterojunctions were evaluated by monitoring the decomposition of rhodamine B (RhB) and 4-chlorophenol (4-CP) in an aqueous solution under visible light irradiation, respectively. Fig. 8ac show the photodegradation of RhB

and 4-CP dyes as a function of irradiation time for the various the 2D BTO and 2D/2D CN/BTO nanosheet heterojunctions. The results for RhB and 4-CP degradation show that after visible-light irradiation, the photocatalytic activities for the CN/BTO samples increased with the increase of CN content from 5wt% to 15wt%. However, the photocatalytic performance decreased with the increase of CN content up to 20wt%. Currently, owe to the photosensitization effect of dye RhB under visible light, we have conducted the photocatalytic performance of blank experiment in the absence of catalyst,[36] indicating that the photocatalytic experiment over blank experiment in the absence of catalyst shows negligible photoactivity for degradation of RhB under identical reaction conditions (Fig. S9). In comparison, the 15wt% CN/BTO photocatalysts exhibited the most pronounced photocatalytic activity with the highest RhB and 4-CP degradation efficiencies of about 98.0% (irradiation for 20 min) and 98.2% (irradiation for 60 min), respectively. These results suggest that the synergistic effect of CN/BTO heterojunction can effectively enhance the photocatalytic activity of CN and BTO nanosheets through the photoinduced interfacial charge transfer. For a better comparison of the photocatalytic efficiency of the above photocatalysts, the kinetic analyses of degradation of RhB and 4-CP are given in Fig. 8bd through a pseudo-first-order reaction model: $\ln(C_0/C) = Kt$, where K is the apparent first-order rate constant (min^{-1}); t is the visible light irradiation time.[33] It can be seen that the linearity between $\ln(C_0/C)$ and time are good for all the photocatalysts,

implying that the photocatalytic degradation of RhB and 4-CP in aqueous suspensions can be described by pseudo-first-order reaction dynamics. As observed in Fig. 8bd, the apparent rate constant of the heterojunction nanosheets increases with increasing the CN nanosheet contents from 5wt% to 15wt%. Nevertheless, when the CN nanosheet content is higher than 20wt%, a further increase in CN content causes a rapid decrease in the apparent rate constant due to the reduction light absorption of BTO nanosheets shielded by CN nanosheets. The recycling experiment of RhB and 4-CP photodegradation indicates good stability of the CN/BTO photocatalyst during the photocatalytic reaction (Fig. S5), which has been confirmed by XRD pattern of the CN/BTO photocatalyst after photocatalytic reaction (Fig. S6).

The exceptional enhancement of the photocatalytic performance for CN/BTO heterojunctions should be ascribed to several points. The assemblage of CN/BTO hybrids forms a uniquely 2D/2D nanostructure, providing a high surface area and a large number of interfaces between CN and BTO species. The high surface areas and profuse interfaces are accessible to the outer environment, and provide numerous active sites for the photodegradation of dye molecules. So, the various samples presented the high absorption activities due to the high surface area (Fig. S7 and S8). Currently, the O-vacancy in the hybrid plays a pivot role upon the photocatalytic activities (Fig. S9). More intriguingly, the O-vacancy confined in BTO coupled with carbon nitride showed the improvement of photodegradation properties that is higher than that of simple mixture of C_3N_4 and BTO (Fig. S9).

Thus, the superior photocatalytic performance is firstly attributed to the synergistic effect between the 2D nanostructure and the O-vacancy confined in the BTO nanosheets as well as the high surface area of CN and BTO. Then, compared to the absorption and degradation properties of CN/BTO samples, the enhancement of photocatalytic performance is mainly ascribed to the fast charge transfer in the CN/BTO. To provide the evidence on the photoinduced interfacial charge transfer process, the steady-state and transient photoluminescence (PL) spectroscopy of CN/BTO were investigated in comparison with those of pure BTO and 15wt% CN/BTO. As shown in Fig. 9a, the BTO nanosheets exhibit a strong emission peak at around 530 nm. However, the intensity of this emission peak for CN/BTO dropped significantly, demonstrating that the recombination of photoinduced charge carrier is inhibited greatly by the interfacial charge transfer between g-C_3N_4 and $Bi_{20}TiO_{32}$. This process was further confirmed by the time-resolved transient PL spectroscopy. As shown in Fig. 9bc, the emission decay data can be fitted by exponential kinetics for which these components are derived. Interestingly, the 15wt% CN/BTO nanosheet heterojunctions (τ_1= 5.11 ns, A_1=64.94%; τ_2= 35.17 ns, A_2=31.29%) yield the longest decay time as compared with the intrinsic BTO nanosheets (τ_1= 5.11 ns, A_1=64.94%; τ_2= 35.17 ns, A_2=31.29%), indicating an accelerated charge transfer mechanism induced by the modification of the CN nanosheets.[37]

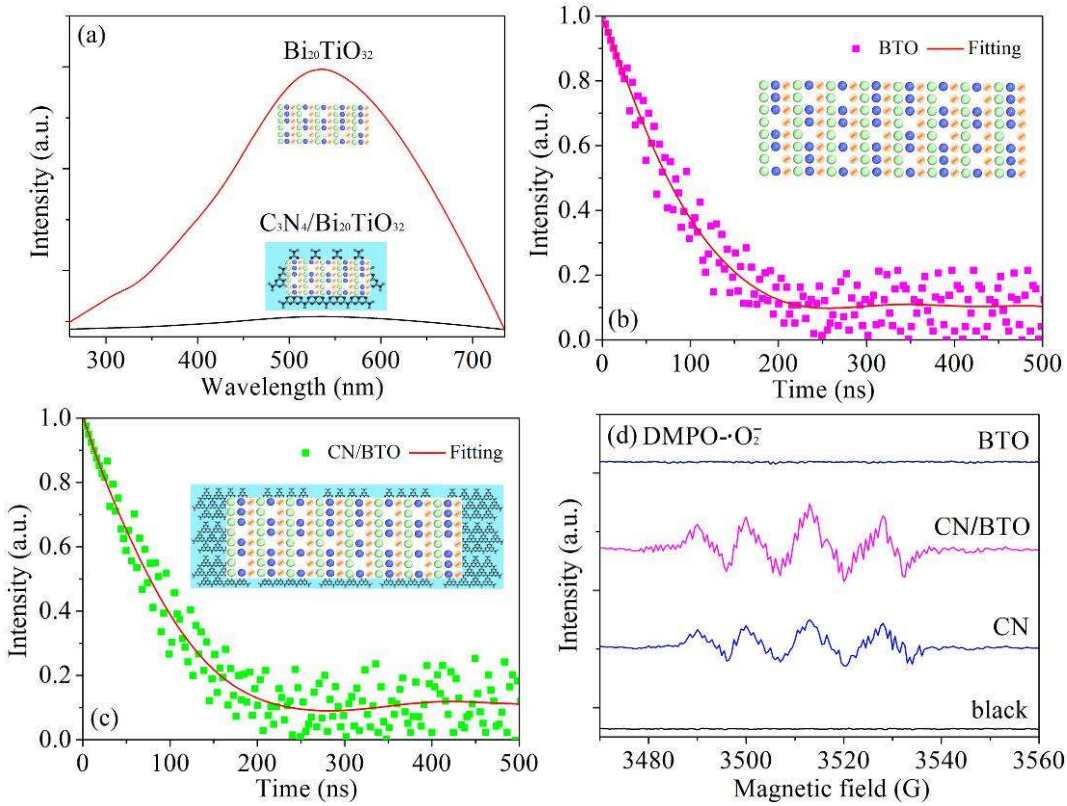

Fig. 9 (a) PL spectra of 15wt% CN/BTO heterojunctions and BTO nanosheets; (bc) ns-level time-resolved PL spectra monitored at 435 nm under 340 nm excitation for BTO and 15wt% CN/BTO heterojunction, (d) ERS signals of the DMPO-•O_2^- with irradiation for 20 s in methoal dispersion.

Although the main evidence of charge transfer of the CN/BTO heterojunctions has been confirmed, it is still necessary to ascertain the migrated channel of the photogenerated electrons and holes. According to the band gap structures of BTO and CN, the separation processes of photoexcited electron-hole can be described in Fig. 10, respectively. With regard to the charge carriers of CN/BTO photocatalyst transfer, the electrons in the CB of CN will migrate to the CB of BTO, and holes in

the VB of BTO will migrate to the VB of CN. Because the accumulated electrons in the CB of BTO can not reduce O_2 to yield $\bullet O^{2-}$, and the holes in the VB of CN can not oxidize OH to give •OH, which has been confirmed by the ESR signals of DMPO-$\bullet O_2^-$ for different samples (Fig. 9d). Currently, it is clear that the characteristic peaks of DMPO-•OH could be observed in the curves of BTO, 15wt% CN/BTO and CN and blank (Fig. S10). There was no DMPO-•OH adducts in dark conditions. It is demonstrated that •OH radicals were generated on these samples after illumination. Thus, the current charge carrier process of CN/BTO heterojunctions is not favorable for the traditional model. However, the Z-scheme charge transfer in the CN/BTO system was proposed according to the main oxidative species in the photocatalytic process of CN/BTO heterojunctions. As a result, the electrons in the CB of CN, which have more negative potential, reduce the molecular oxygen to yield $\bullet O^{2-}$; and the holes in the VB of BTO, which have more positive potential, generate abundant active •OH radicals. Namely, a typical Z-scheme photocatalyst is favorable for the production of $\bullet O^{2-}$ and •OH reactive species, which is in agreement with the analysis of the photocatalytic activity and reactive species of the CN/BTO heterojunctions (Fig. 10). The intimate and large contact interfaces favor the effective charge transfer, leading to the higher photocatalytic activity of the 2D/2D heterojunctions. In terms of the safety and the non-secondary pollution to the environment, our composites are high-performance nanoscale photocatalysts. These composites with high photocatalytic activity could be beneficial to industrial applications to eliminate the organic pollutants from

waste water.[38-40] Especially, we envision that it will open new windows to rationally designing hybrid materials for environmental remediation applications.

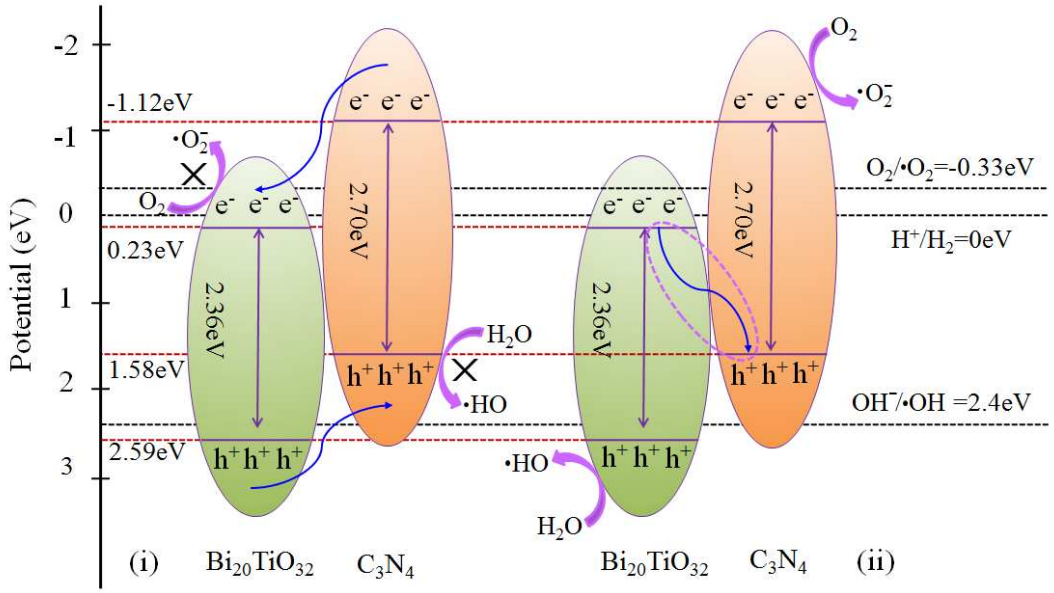

Fig. 10 Schematic illustration of photogenerated electron-hole separation and transportation for 2D/2D CN/BTO nanosheets heterojunctions.

Conclusion

We have designed and fabricated the first 2D/2D heterojunctions between carbon nitride and oxygen-vacancy confined in bismuth titanate mesoporous nanosheets. The effect of different addition ratios of C_3N_4 on the photocatalytic performance of CN/BTO heterojunctions was systematically investigated, and the photocatalytic activities of the hybrids was discussed with respect to the light-absorbance properties, interaction between C_3N_4 and oxygen-vacancy confined in bismuth titanate mesoporous nanosheets, and photoluminescence spectra. At an optimal

ratio of 15wt% carbon nitride, the 2D/2D heterojunctions can serve as an efficient visible-light-driven photocatalyst for pollutant transformations of rhodamine B (RhB) and 4-chlorophenol (4-CP). Based on the steady-state and transient photoluminescence spectra and electron spin resonance technology, the Z-scheme energy-transfer mechanism is identified and the photogenerated charge carriers in the 2D/2D heterojunctions display the prolonged lifetime and higher separation than those in carbon nitride and bismuth titanate alone. This novel 2D/2D heterojunctions could be beneficial to industrial applications to eliminate the organic pollutants from waste water in environmental remediation fields.

Acknowledgements

This work was supported by the Fundamental Research Funds for the Central Universities (FRF-TP-14-110A2).

Supporting Information Available: FT-IR, Raman spectra, XRD patterns and photocatalytic performance.

References

1. L. Thompson , J. T. Jr. Yates, Chem. Rev., 2006 , 106, 4428.

2. X. Chen, L. Liu, P. Y. Yu, S. S. Mao, Science, 2011, 331, 746.

3. N. S. Lewis, D. G. Nocera, Proc. Natl Acad. Sci. USA, 2006, 103, 15729–15737.

4. Z. G. Zou, J. H. Ye, K. Sayama, H. Arakawa, Nature, 2001, 414, 625.

5. H. Yamashita, M. Harada, J. Misaka, M. Takeuchi, K. Ikeue, M. Anpo. J. Photochem. Photobiol. A, 2002, 148, 257.

6. J. G. Hou, Z. Wang, C. Yang, H. J. Cheng, S. Q. Jiao, H. M. Zhu, Energy Environ. Sci., 2013, 6, 3322.

7. X. C. Wang, K. Maeda, A. Thomas, K. Takanabe, G. Xin, J. M. Carlsson, K. Domen and M. Antonietti, Nature Mater., 2009, 8, 76.

8. Z. G. Yi, J. H. Ye, N. Kikugawa, T. Kako, S. X. Ouyang, H. Stuart-Williams, H. Yang, J. Y. Cao, W. J. Luo, Z. S. Li, Y. Liu, R. L. Withers, Nat. Mater., 2010, 9, 559.

9. J. G. Hou, C. Yang, H. J. Cheng, S. Q. Jiao, O. Takeda, H. M. Zhu, Energy Environ. Sci., 2014, 7, 3758.

10. R. Asahi, T. Morikawa, T. Ohwaki, K. Aoki, Y. Taga, Science, 2001, 293, 269.

11. J. G. Hou, R. Cao, Z. Wang, S. Q. Jiao, H. M. Zhu, R.V. Kumar. Appl. Catal. B 2011, 104, 399.

12. J. G. Hou, Y. F. Qu, D. Krsmanovic, R. V. Kumar, J. Nanopart. Res., 2010, 12, 1797.

13. J. G. Hou, Z. Wang, C. Yang, W. L. Zhou, S. Q. Jiao, H. M. Zhu, J. Phys. Chem. C, 2013, 117, 5132.

14. J. G. Hou, Y. F. Qu, D. Krsmanovic, C. Ducati, D. Eder, R. V. Kumar, J. Mater. Chem., 2010, 20, 2418.

15. J. G. Hou, Y. F. Qu, D. Krsmanovic, C. Ducati, D. Eder, R. V. Kumar, Chem. Commun., 2009, 26, 3937.

16. H. F. Cheng, B. B. Huang, Y. Dai, X. Y. Qin, X. Y. Zhang, Z. Y. Wang, M. H. Jiang, J. Solid. State. Chem., 2009, 182, 2274.

17. J. Zhang, Q. Xu, Z. C. Feng, M. J. Li, C. Li, Angew. Chem. Int. Ed., 2008, 47, 1766.

18. M. A. Henderson, I. Lyubinetsky, Chem. Rev., 2013, 113, 4428.

19. Y. F. Sun, S. Gao, Y. Xie, Chem. Soc. Rev., 2014, 43, 530.

20. Y. Zheng, J. Liu, J. Liang, M. Jaroniec, S. Z. Qiao, Energy Environ. Sci., 2012, 5, 6717.

21. X. S. Zhou, B. Jin, L.D. Li, F. Peng, H. J. Wang, H. Yu, Y. P. Fang, J. Mater. Chem., 2012, 22, 17900.

22. J. G. Hou, H. J. Cheng, O. Takeda and H. M. Zhu, Energy Environ. Sci., 2015, 8, 1348.

23. Y. J. Wang, R. Shi, J. Lin, Y. F. Zhu, Energy Environ. Sci., 2011, 4, 2922.

24. L. Ge, C. C. Han, J. Liu, Appl. Catal. B., 2011, 108-109, 100.

25. J. X. Low, S. W. Cao, J. G. Yu, S. Wageh, Chem. Commun., 2014, 50, 10768.

26. N. Tian, H. W. Huang, Y. He, Y. X. Guo, T. R. Zhang, Y. H. Zhang, Dalton T., 2015, 44, 4297.

27. F. Dong, Z. W. Zhao, T. Xiong, Z. L. Ni, W. D. Zhang, Y. J. Sun, W. K. Ho, ACS Appl Mater Interfaces, 2013, 5, 11392.

28. Z. Y. Zhang, J. D. Huang, M. Y. Zhang, Q. Yuan, B. Dong, Appl. Catal. B, 2015, 163, 298.

29. S. C. Han, L. F. Hu, Z. Q. Liang, S. Wageh, A. A. Al-Ghamdi, Y. S. Chen, X. S. Fang, Adv. Funct. Mater., 2014, 24, 5719.

30. L. M. Sun, X. Zhao, C. J. Jia, Y. X. Zhou, X. F. Cheng, P. Li, L. Liu, W. L. Fan, J. Mater. Chem., 2012, 22, 23428.

31. H. Zhang, R. L. Zong, Y. F. Zhu, J. Phys. Chem. C, 2009, 113, 4605.

32. Q. J. Xiang, J. G. Yu, M. Jaroniec, J. Phys. Chem. C., 2011, 115, 7355.

33. J. X. Sun, Y. P. Yuan, L. G. Qiu, X. Jiang, A. J. Xie, Y. H. Shen, J. F. Zhu, Dalton Trans., 2012, 41, 6756.

34. F. C. Lei, Y. F. Sun, K. T. Liu, S. Gao, L. Liang, B. C. Pan, Y. Xie, J. Am. Chem. Soc. 2014, 136, 6826.

35. S. Q. Zhanga, Y. X. Yang, Y. N. Guo, W. Guo, M. Wang, Y. H. Guo, M. X. Huo, J. Hazard. Mater., 2013, 261, 235.

36. L. Yuan, M. Q. Yang, Y. J. Xu, Nanoscale, 2014, 6, 6335.

37. M. A. Mahmoud, W. Qian, M. A. El-Sayed, Nano Lett., 2011, 11, 3285.

38. M. Q. Yang, N. Zhang, M. Pagliaro, Y. J. Xu, Chem. Soc. Rev., 2014, 43, 8240-8254.

39. N. Zhang, Y. H. Zhang, Y. J. Xu, Nanoscale, 2012, 4, 5792.

40. M. Q. Yang, Y. J. Xu, Phys. Chem. Chem. Phys., 2013, 15, 19102.

Graphical Abstract

This work will shed light on the rational design of more complex 2D/2D heterojunctions with the Z-scheme energy-transfer mechanism.